Nanoscale Segregation Behavior and High-Temperature Stability of Nanocrystalline W-20 at.% Ti

Tongjai Chookajorn and Christopher A. Schuh*

Department of Materials Science and Engineering, MIT

77 Massachusetts Avenue, Cambridge, MA 02139, USA

***Corresponding Author:** C.A. Schuh, e-mail address: schuh@mit.edu, phone: 617-253-6901

Abstract:

Nanocrystalline W powders with ~20 nm average grain size are produced by high-energy ball milling and exposed to a target consolidation temperature of 1100°C. After one week, unalloyed W exhibits substantial grain growth where a W alloy with 20 at.% Ti retains its nanoscale structure. A heterogeneous distribution of Ti is observed by independent characterization methods including scanning transmission electron microscopy, energy dispersive spectroscopy, and atom probe tomography. This heterogeneous solute distribution is different from the expected homogeneous solid solution based on bulk W-Ti phase diagrams. Using a Monte Carlo simulation that includes the possibility of grain boundary segregation and allows grain boundaries as potential equilibrium states, a complex nanoscale structure of Ti around W-rich crystallites is explicitly reproduced. This simulated structure has both grain size and extrema in local Ti content in line with the experimental observations.

Keywords: Nanostructured metals; Nanocrystalline alloys; Thermodynamic stability; Grain boundary segregation

1. Introduction

The thermodynamics of binary alloys traditionally focuses only on material configurations that comprise "bulk" or crystalline regions, such as homogeneous solid solutions, phase-separated solid solutions, and intermetallic compounds. However, when the characteristic internal length scale of the system (such as the grain size) is reduced into the nanoscale, the interfaces become increasingly relevant, and can enable different configurations that are not explicitly accounted for in conventional bulk thermodynamics. One important aspect of thermodynamics in nanostructured systems that gives rise to many unique material characteristics and has been found ubiquitous in the experimental literature is grain boundary segregation [1-6]; minority elements in a polycrystal frequently prefer to segregate at grain boundaries rather than being dissolved in the grain interior. Considering the presence or absence of such interfaces as an additional possible degree of freedom for the alloy configuration naturally connects grain boundary solute segregation to nanosystem thermodynamics.

For certain alloy systems with a positive enthalpy of grain boundary segregation, ΔH^{seg}, a nanocrystalline grain structure can be maintained in equilibrium when the total free energy, G, is minimized at a certain grain size [7-12]. This requires sufficient solute enrichment, Γ, at grain boundaries such that the derivative of free energy with respect to grain boundary area, $\frac{\mathrm{d}G}{\mathrm{d}A}$, can become zero according to:

$$\frac{\mathrm{d}G}{\mathrm{d}A} = \frac{\mathrm{d}(\Sigma \mu_{\mathrm{i}} N_{\mathrm{i}})}{\mathrm{d}A} + \gamma_0 - (\Gamma + A\frac{\mathrm{d}\Gamma}{\mathrm{d}A})(\Delta H^{\mathrm{seg}} + \mathrm{k}T\ln X) \qquad (1)$$

where the chemical potential term $\Sigma\mu_{\mathrm{i}}N_{\mathrm{i}}$ (i.e., the sum over all atomic species i, each with chemical potential μ_{i} and number of atoms N_{i}) captures the chemical contribution (including the bulk atomic configurations), γ_0 is the intrinsic energy penalty of grain boundaries in unalloyed solvent, kT is the thermal energy, and X is the solute content. To attain a stable polycrystalline state with a finite grain size, $\frac{\mathrm{d}G}{\mathrm{d}A} = 0$ is required and is accompanied by reduction in the grain boundary formation energy, γ, to a negative value via $\gamma = \gamma_0 - \Gamma(\Delta H^{\mathrm{seg}} + \mathrm{k}T\ln X)$ [11, 12]. Based on Eq. (1), this condition is promoted by systems with a higher tendency for solute to segregate to grain boundaries than to mix in the grain interior, and by abundant solute excess at grain boundaries. An analysis of relative magnitudes of bond energies in Refs. [11, 12] indicates that alloy combinations with a large enthalpy of grain boundary segregation relative to enthalpy

of mixing (or a reasonably negative grain boundary interaction energy) are generally the systems with stable nanostructured states.

One alloy system identified in our earlier work that might meet the above conditions is the W-Ti system, where Ti is the minority element and is expected to have a positive enthalpy of grain boundary segregation as well as a relatively modest enthalpy of mixing in W (i.e., Ti atoms should prefer grain boundary sites). In our preliminary letter [13], nanocrystalline W-Ti alloy powder with enhanced thermal stability was introduced; with a 20 at.% addition of Ti, we reported that a nanoscale grain structure (grain size of ~20 nm) could be retained at the target consolidation temperature of 1100°C [14, 15] for one week. Even though the conventional equilibrium phase diagram for this system expects a single-phase solid solution of W and Ti for these conditions, we observed a well-defined nanostructure with patterns of solute enrichment and depletion throughout the structure. These results thus qualitatively aligned with the notion presented around Eq. (1), i.e. the unique configurations accessible in nanostructured alloys may be thermodynamically preferred over the conventional bulk equilibrium.

The results in our preliminary report [13] were presented in the spirit of an initial demonstration worthy of greater study and needing a more detailed connection to theory; this is our purpose in the present paper. Here we explore in more detail the segregation behavior in nanostructured W-20 at.% Ti alloy using multiple independent characterization methods and also a thermodynamic Monte Carlo simulation that explicitly considers the possible contribution from grain boundaries on the overall material configuration. The comparison between experimental results and simulated structure underlines the connection between thermodynamics in nanoscale systems and attainment of nanocrystalline materials with enhanced high-temperature stability.

2. Methods

A nanocrystalline W-Ti alloy was produced by high-energy ball milling from APS 1-5 μm W powder and 150-mesh Ti powder, both with 99.9% purity and purchased from Alfa Aesar. The starting W-20 at.% Ti powder mixture and 1 wt.% stearic acid process control agent were introduced into a tungsten carbide vial with tungsten carbide media at a 5 to 1 ball-to-powder ratio and ball milled for six hours in a glove box under an argon atmosphere using a SPEX 8000M mill. The resulting alloy powder as well as an unalloyed tungsten specimen prepared

using the same milling procedure were tested for thermal stability by annealing at 1100°C for one week (168 hours) before being quenched to room temperature.

JEOL 2010F and 2011 transmission electron microscopes (TEM) operated at 200 kV were used for bright- and dark-field imaging and also for selected-area electron diffraction. Microscopy specimens were prepared from loose powder without any binding material, using the lift-out method in an FEI Helios focused ion beam (FIB). The scanning transmission electron microscopy (STEM) and energy-dispersive spectroscopy (EDS) capabilities of the JEOL 2010F TEM were used for diffraction- and atomic-contrast imaging and also for elemental mapping of the pre- and post-annealing structures. The chemical distributions of W and Ti were examined using the STEM-EDS technique and the Cliff-Lorimer equation [16] was used to quantify the extent of chemical segregation.

In addition, the chemical configuration of the W-20 at.% Ti alloy after the equilibration at 1100°C was also characterized by the atom probe tomography (APT) technique. The APT specimen was produced by the FIB lift-out method from loose powder, and the atom probe procedure was performed in a Cameca local electrode atom probe (LEAP-4000X HR) under the laser pulse mode with the initial pulse frequency of 50 kHz at the pressure of 4.9×10^{-11} torr at 55 K. Approximately 1.4×10^{6} detector events were collected and 9.8×10^{5} atoms in the stable pulsing regime were used for further analysis.

3. Grain Structure

3.1. Pre-Annealing Structure

Following six hours of ball milling, both the unalloyed and alloyed powders became nanocrystalline with similar as-milled structures, as illustrated by the uniform nanoscale grain structures in the bright-field TEM images in Fig. 1(a)-(b). Each crystal under the Bragg condition produces diffraction contrast in the inset dark-field TEM images in Fig. 1(a)-(b), which highlight a few typical grains in each case. Similarly, the diffracted signals from these nanocrystalline grains constitute ring-like electron diffraction patterns in Fig. 1(c)-(d) characteristic of fine-grained polycrystalline materials. The diffraction patterns can be indexed by body-centered cubic (BCC) W reflections, in line with an independent assessment by X-ray diffractometry; the as-milled W-Ti alloy is a solid solution with no evidence of second phases of W or Ti. Minor traces

of diffraction spots around the W(110) rings were found to be from the platinum protection layer deposited before the FIB lift-out procedure. By tracing the grain perimeters and calculating the average grain size from area-equivalent circle diameters, the grain size histograms in Fig. 3 show the refined nanoscale grain sizes in both W-Ti alloy and unalloyed W, the average values being about 22 and 17 nm, respectively.

3.2. Post-Annealing Structure

After a one-week anneal at 1100°C, the unalloyed W exhibits substantial grain coarsening to the average grain size of ~600 nm, as shown by the FIB image in Fig. 2(a). Under the same annealing condition, the W-20 at.% Ti alloy in Fig. 2(b) maintains a much finer average grain size of 24 nm. The 25-fold difference between these cases is more clearly visible from the comparison of grain size histograms in Fig. 3. Without alloying, nanocrystalline tungsten undergoes severe grain coarsening with the larger tail of the grain size distribution reaching well into the micrometer scale. However, with the addition of titanium, the grain structure remains on the nanometer scale and is not significantly different from that of the pre-annealing structure. The complete ring-like electron diffraction patterns from the post-annealing W-20 at.% Ti specimen in Fig. 2(d) also closely match those of the pre-annealing structure in Fig. 1(d). In contrast, the diffraction patterns from the post-annealing unalloyed W in Fig. 2(c) appear scattered and do not form a complete ring as a result of its larger average grain size and therefore a lower number of grains under the diffracting condition. Furthermore, the relatively large crystallites also produce more evident reflections from lower symmetry planes in Fig. 2(c) compared to the fine-grained structure in Fig. 2(d). In both cases, the electron diffraction patterns are indexed with BCC reflections; there is no clear evidence of any second phase in these patterns.

4. Chemical Distribution

The bulk phase diagram for the W-Ti system shows a large miscibility gap between these elements, but with a relatively low critical temperature of ~1200°C. Under the conditions of our annealing (1100°C) the system lies considerably above the solvus by ~600°C; the stable bulk state is expected to be a homogeneous solid solution [17, 18]. On the other hand, the premise of Eq. (1) and the concept of thermodynamic grain stabilization rest upon the possibility of a nonuniform chemical distribution effected by the availability of interfacial sites in the system.

Accordingly, the increased stability of the W-20 at.% Ti alloy might be expected to be accompanied by nonuniform solute distribution, to which we turn our attention in this section.

4.1. Pre-Annealing Structure

A bright-field STEM image, showing Ti-rich areas in brighter contrast and W-rich areas in darker contrast, as well as EDS elemental distribution maps of the as-milled structure of the W-20 at.% Ti alloy are shown in Fig. 4(a). In the as-milled, pre-annealed state, the chemical distribution is not perfectly uniform, but generally exhibits the character of a system well-mixed to the atomic level. Compositional line profiles of Ti are shown in Fig. 4(b), and these should be considered semi-quantitative due to fluctuations in sample thickness, etc. These line scans display some minor fluctuations of Ti content around the nominal 20 at.% concentration, but these do not appear correlated to the corresponding STEM image contrast.

At room temperature, the bulk W-Ti phase diagram shows that Ti and W are immiscible, with the solubility of Ti in W being below 12 at.% and that of W in Ti being near zero [17, 18]. As expected, high-energy ball milling is an entropy-inducing process that can force the mixing of these elements to a much greater degree than expected from these bulk solubilities [19-29]; the average solution composition of ~20 at.% Ti in W is within the bulk miscibility gap at room temperature. While Fig. 4 reveals some subtle fluctuations in the chemical distribution at the nanoscale, ball milling is not completely randomizing in general [19-33], and these fluctuations are reflective of the randomizing tendency of the milling process in competition with the strong chemical and mechanical tendencies of Ti and W to avoid mixing. All of the evidence of diffraction (Fig. 1) and chemical mapping (Fig. 4) shows clear intermixing to the atomic scale, and the forced formation of a single-phase BCC solid solution.

4.2. Post-Annealing Structure

A significantly inhomogeneous distribution of Ti is evident in the STEM images and EDS maps of the W-20 at.% Ti alloy after annealing at 1100°C for a week, as shown in Fig. 5(a). The Ti composition profiles from EDS in Fig. 5(b) show a correlated fluctuation in Ti content with the visible tungsten regions identified by the darker contrast in the corresponding STEM images. The local Ti content decreases below the nominal composition of 20 at.% close to the center of dark W-rich regions and rises above 20 at.% in the adjacent areas. Although STEM images can reveal the contrast between heavy and light elements, two adjacent tungsten grains

with different crystal orientations may not be as clearly resolved as by the diffraction contrast in the TEM images in Fig. 2(b). The EDS compositional profile shows the value of Ti content varying between about 5 and 60 at.%. Similar Ti composition profiles are observed from the two STEM images obtained from different regions of the sample in Fig. 5(b).

In the STEM-based analysis above, there is always an implicit source of error from averaging the chemical signal over the thickness of the specimen, which may include multiple grains. The annealed W-20 at.% Ti sample is therefore further analyzed using atom probe tomography, which allows investigation of the full volume distributions of W and Ti atoms without the area projection of chemical signals. The APT results are first shown in a top-down view of the overall volume distributions in Fig. 6(a), in order to compare with the through-thickness STEM measurements. And while the distribution of W atoms appears more uniform in Fig. 6(b), both Ti-rich and Ti-depleted regions are present in the Ti distribution map in Fig. 6(c). The overall distributions of both types of atoms presented in the mixed elemental map in Fig. 6(a) resemble those observed earlier by the STEM-EDS method in Fig. 5. For the volume analyzed in the selected field of view, the global measured concentration of Ti with respect to W is about 35.6 at.%, which suggests that this local sample is in a titanium-rich region of the specimen.

A more quantitative interpretation of the APT results is provided by the compositional isosurfaces (or isoconcentration surfaces) in Fig. 7(a) and (b). The regions enclosed by the red surfaces are enriched above the nominal 20 at.% Ti concentration, and the complementary blue regions have W content higher than 80 at.%. The volume distribution of atoms can also be presented by a combination of multiple isosurfaces into an isovolume presentation in Fig. 7(c) and (d), where the colors indicate the relative Ti content at each point in the volume. Quantitative compositional line profiles of Ti content are shown in Fig. 7(e) and (f), taken along the horizontal and vertical axes of the specimen, respectively. These line scans display local peaks in Ti concentration as high as about 60 at.%, and valleys as low as ~0 at.% Ti. The length scale of these variations is on the order of 20-25 nm, but this is qualitative given the small size of the APT specimen.

5. Kinetics

The above results show that the W-20 at.% Ti alloy remains in a nanostructured state (~20 nm grain size) and has a decidedly nonuniform solute distribution after one week at 1100°C. The amplitude of the solute fluctuations is extremely large, ranging from a few to ~60 at.% Ti depending upon position, and validated by both STEM-EDS and APT results. Both of these aspects (the nanostructural length scale and the nonuniform solute distribution) are unexpected based on the bulk phase diagram, so it is a relevant question as to whether one week at 1100°C is sufficient time-at-temperature for the system to attempt to reach equilibrium.

Interdiffusivity of a binary alloy, $\widetilde{D}$, can be estimated using Darken's equation [34, 35], which combines intrinsic diffusivity D of the two components using their mole fraction X by:

$$\widetilde{D} = X_{\mathrm{W}} D_{\mathrm{Ti}} + X_{\mathrm{Ti}} D_{\mathrm{W}} \tag{2}$$

The analysis can be further simplified by assuming an ideal solution behavior of bulk W-20 at.% Ti solid solution at 1100°C, and hence using self-diffusivity of each chemical species for the estimation of interdiffusivity. In a nanocrystalline structure, diffusion occurs through the lattice (with diffusivity D_{vol}), grain boundaries (with D_{gb}), as well as triple junctions (with D_{tj}), and a composite average of these structural elements that respects their geometrical arrangement can be written [36]:

$$D_{\mathrm{eff}} = D_{\mathrm{vol}} + g(d)\left[\frac{2H_{\mathrm{gb}}\delta}{d}\left(D_{\mathrm{gb}} - D_{\mathrm{vol}}\right) + \frac{H_{\mathrm{tj}}\delta^2}{d^2}\left(D_{\mathrm{tj}} - D_{\mathrm{vol}}\right)\right] \tag{3}$$

where

$$\mathrm{g}(d) = \frac{2H_{\mathrm{gb}}\delta^3 + 2H_{\mathrm{tj}}\delta d^2}{6H_{\mathrm{gb}}\delta^3 - \left(2H_{\mathrm{gb}}^2 - 3H_{\mathrm{tj}}\right)\delta d^2 - 3H_{\mathrm{gb}}H_{\mathrm{tj}}\delta^2 d - H_{\mathrm{tj}}^2\delta^3} \tag{4}$$

is a geometrical parameter comprising an average dilute-limit grain boundary thickness, δ (taken to be 0.5 nm here), and the two grain shape factors are assigned using values for a log-normal size distribution of Voronoi polyhedra, H_{gb} = 2.9105 and H_{tj} = 2.5259 [36]. The effective diffusivity D_{eff} thus represents the combined diffusional transport through the pathways denoted by the subscripts and is influenced by the average grain size d of a polycrystal.

Combining Eqs. (2)-(4) allows a reasonable estimation of both W effective diffusivity and W-Ti interdiffusivity in a nanocrystalline ideal solution, and at T = 1100°C the relevant inputs to the analysis are $D_{W,vol}$ = 3.9x10^{-26} m^2/s [37], $D_{W,gb}$ = 9.2x10^{-17} m^2/s [37], and $D_{W,tj}$ = 9.2x10^{-12} m^2/s based on the typical $D_{gb,BCC}$ to D_{tj} ratio at 0.37 homologous temperature [36]. The self-diffusivity of Ti at 1100°C is $D_{Ti,BCC}$ = 4.1x10^{-13} m^2/s [38].

The effective self-diffusivity D_{eff} of tungsten is shown as a function of grain size in Fig. 8, along with the individual contributions to it. The increase in tungsten's polycrystalline diffusivity becomes important when the grain size is decreased below 100 nm, where D_{eff} exceeds the value of $D_{W,gb}$. The total chemical diffusion distance after one week can be estimated as $L \approx (Dt)^{1/2}$ with diffusion time t = 168 hours, and is presented as a function of grain size on the secondary axis of Fig. 8. For all grain sizes below 100 nm, the effective W diffusion distance L is larger than 1 μm. By combining $D_{W,eff}$ and $D_{Ti,BCC}$ using Eq. (2), the W-Ti interdiffusivity and the one-week chemical interdiffusion distance shown in Fig. 8 reveal an expected interdiffusion distance exceeding 100 μm, higher than of the self-diffusivity of W due to the high mobility of Ti compared to W.

We conclude that the time-at-temperature provided under our annealing conditions should kinetically allow for large-scale redistribution of W and Ti atoms by the end of the equilibration process. Both grain coarsening and intermixing of W and Ti atoms should be possible given the equilibration time, should these structural changes be energetically favored. The unalloyed W specimen underwent the expected coarsening with the final grain structure extending to micrometer in size. Nonetheless, our experimentally observed W-20 at.% Ti structure did not coarsen nor intermix.

6. Thermodynamics

Since the above kinetic analysis suggests that the time-at-temperature of our annealing process was sufficient to allow the microstructure to relax over scales much larger than the grain size, it is possible that the nanostructure is stabilized via the thermodynamic considerations described in the introduction and underlying Eq. (1). This implies a tendency for Ti atoms to prefer grain boundary sites in W, i.e., a positive enthalpy of grain boundary segregation, which may be driven by a number of considerations including mismatches in chemical, interfacial, and

elastic (size misfit) energies. Murdoch and Schuh [39] presented a modified Miedema model to estimate the dilute-limit grain boundary segregation enthalpy on the basis of such effects using:

$$\Delta H^{\text{seg}} = \frac{0.71}{6}\Delta H^{\text{int}}_{\text{TiinW}} + \frac{0.71}{6}\left(c_0\gamma^{\text{S}}_{\text{W}}\Omega^{\frac{2}{3}}_{\text{W}} - c_0\gamma^{\text{S}}_{\text{Ti}}\Omega^{\frac{2}{3}}_{\text{Ti}}\right) + \Delta E_{\text{el}} \qquad (5)$$

The chemical effect is accounted for by the chemical interaction energy of Ti atoms in W, captured by the term $\frac{0.71}{6}\Delta H^{\text{int}}_{\text{TiinW}}$ which is approximated from the chemical contribution in the enthalpy of mixing to be about 2 kJ/mol for our system [13, 40]. The mismatch in interfacial energies is presented by the difference between the values of $c_0\gamma^{\text{S}}_{\text{i}}\Omega^{\frac{2}{3}}_{\text{i}}$ for each component i, where c_0 is a semiempirical constant taken as 4.5x10^8 [39], $\gamma^{\text{S}}_{\text{i}}$ is the surface energy, and Ω_{i} is the atomic volume. With input values of $\gamma^{\text{S}}_{\text{W}}$ = 3.675 J/m^2 [41], $\gamma^{\text{S}}_{\text{Ti}}$ = 1.7 J/m^2 [42], Ω_{W} = 9.47 cm^3/mol [43], and Ω_{Ti} = 10.64 cm^3/mol [43], we estimate the interfacial energy contribution as being around 44 kJ/mol. The elastic mismatch,

$$\Delta E_{\text{el}} = \frac{24\pi K_{\text{W}} G_{\text{Ti}} r_{\text{W}} r_{\text{Ti}} (r_{\text{W}} - r_{\text{Ti}})^2}{3K_{\text{W}} r_{\text{W}} + 4G_{\text{Ti}} r_{\text{Ti}}}\ , \qquad (6)$$

depends on metallic radii r, bulk modulus K, and shear modulus G of the atomic species denoted by the subscript, and is evaluated to be about 2 kJ/mol (K_{W} = 310 GPa [44], G_{Ti} = 17.5 GPa [45], r_{W} = 1.39 Å [46], and r_{Ti} = 1.47 Å [46]).

Based on the above analysis, the elastic mismatch term and the chemical term are both found to be relatively minor in comparison to the change in grain boundary energy caused by a substitution of Ti for W atoms; to first order the change in grain boundary cohesive energy dominates the segregation tendency of Ti in W. Combining all of the above values together in Eq. (5) gives an estimated average enthalpy of grain boundary segregation of about 50 kJ/mol for Ti in W, which can be used as input to a thermodynamic analysis to further explore the effects of grain boundaries on the expected equilibrium structure of this alloy.

We use a Monte Carlo simulation method introduced in our prior work in Refs. [11, 12] to determine the equilibrium structure of generic binary alloys when grain boundaries are included as possible equilibrium features; here we adapt that method to the specific case of W-20 at.% Ti. Briefly, the method is a latticed-based simulation in which each gridpoint contains a

chemical (atomic identity) and structural (grain number) state variable. A BCC lattice with 400 x 400 x 6 sites and a total of 9.6×10^5 atoms is used, with an equivalent width and length of 126 nm and periodic boundary conditions applied on all three axes. The simulation equilibrates the system by a random sequence of equally probable atom switching and grain switching. The locations of two atoms can be switched to evolve the chemical distribution. Alternatively, the grain number of a grain boundary site can be switched, which allows for grain size evolution and also grain nucleation. The Monte Carlo algorithm evolves both grain and atomic structures by an equilibrium-seeking Metropolis algorithm employed in a simulated-annealing mode, i.e., slow cooling from high temperatures to a target temperature. More details on the method can be found in Refs. [11, 12].

For the present implementation of the model, the bulk like-atom bonds are taken to have energies E_c^{WW} = 486 kJ/mol [47], and E_c^{TiTi} = 255 kJ/mol, estimated using the ratio between the melting points of W and Ti metals. The enthalpy of mixing ΔH^{mix} = 20 kJ/mol is chosen based on the temperature dependent relation ΔH^{mix} = 15115.2 + 3.90656·T[K] J/mol [40], which reproduces the correct critical temperature of the miscibility gap of the W-Ti system (~1000°C). The enthalpy of grain boundary segregation, as noted above, is estimated as ΔH^{seg} = 50 kJ/mol, while unalloyed grain boundaries have energy penalties $\frac{\Omega_W \gamma_{0,W}}{z\delta}$ = 2.6 kJ/mol and $\frac{\Omega_{Ti} \gamma_{0,Ti}}{z\delta}$ = 2 kJ/mol, where $\gamma_{0,W}$ = 1.1 J/m^2, $\gamma_{0,Ti}$ = 0.75 J/m^2, and z is the BCC coordination number of 8. With these material parameters, the bond energies in our alloy system are ordered: $E_{gb}^{WTi} < E_c^{WW} < E_c^{WTi} < E_{gb}^{TiTi} < E_{gb}^{WW}$. A grain boundary bond can exist in a lower energy state with alloying with a preference over grain interior mixing ($E_{gb}^{WTi} < E_c^{WTi}$), and Ti atoms are expected to favor grain boundary sites.

6.1. Bulk Structure

Before considering the influence of grain boundaries, it is instructive to consider the equilibrated bulk structure, forced to evolve without any grain boundaries, as a bulk thermodynamic baseline case. In this case the Monte Carlo simulation produces the expected single-phase solid solution without phase separation or chemical ordering at 1100°C shown in Fig. 9(a), which presents regions with only W atoms in black, those with only Ti atoms in white, and a composition-dependent gradient shade of gray for a W-Ti mixture. Further investigation

can be made by imitating the experimental compositional line scans; the numbers of W and Ti atoms along a horizontal line averaged over 2.5 nm spots through the full thickness are normalized to produce composition profiles. The Ti profile in Fig. 9(b) shows some fluctuation around the nominal 20 at.% concentration, but with no significant local peaks.

6.2. Equilibrium Nanostructure

The Monte Carlo simulation can be applied without the bulk constraint to simulate a fully equilibrated structure with possible incorporation of grain boundaries. The resulting structure is polycrystalline with a complex solute segregation structure as shown in Fig. 10(a), where W atoms appear dark and Ti atoms light. The grain structure is isolated and presented in Fig. 10(b) by grain number-coloring. The most notable feature of this microstructure is the individual W-rich grains, which are visible as ~20-30 nm patches of a single color in Fig. 10(b). These are found to be dilute solid solutions internally (cf. Fig. 10(a)). The composition profile in Fig. 10(c) reveals this quantitatively, and the W-rich grains are found to have an average composition of ~5 at.% Ti.

Between the large W-rich grains is a complex network of "intergranular" material, which is considerably thicker than a single grain boundary, spanning several to several dozen atomic sites in some places. This region is rich in Ti, which can be seen very clearly in the composition-dependent chemical map of Fig. 10(a) and elucidated further by Fig. 10(d), which shows the overall grain structure with a Ti distribution overlay in black. Closer inspection of the composition-dependent Ti map along a horizontal line in Fig. 10(e-f) reveals segregation of Ti atoms where the grain structure is intergranular. The quantitative Ti profile in Fig. 10(c) also confirms a correlated rise in local Ti content in the intergranular region to a maximum of ~55 at.%.

These results visually present a distinct Ti segregation zone around the W-rich grains, with a relatively dilute amount of Ti dissolved in the grain interior. The structure of the Ti-rich regions is unusual and pushes a limit of the simulation; it involves many single-pixel "grains", which have no tendency to grow. The titanium-rich region so strongly prefers a grain boundary environment that it evolves to this lattice-equivalent of an "amorphous" structure. The implication here is that W-Ti may have an amorphization tendency that is a result of its grain boundary segregation preference, a concept explored in an earlier general analytical analysis (not

specifically applied to W-Ti) by Murdoch and Schuh [48] and others [8, 49, 50]. The present simulation results line up with the analytical predictions of that study, and suggest that in sufficiently non-dilute nanocrystalline alloys, "grain boundaries" may thicken into amorphous-like films to satisfy the bonding preference of the solute. The problem could be approached by allowing the grain boundary thickness to vary in the analytical model, although the inclusion of both "thin" grain boundaries and "bulk" amorphous regions in the approach of Ref. [48] permits both environments to exist in competition; this is more akin to the MC results in the present result, which evolve "thin" and "thick" disordered regions as energetics prefers. This is a topic worthy of further study and will be a focus of some of our future work. For the purposes of the present paper, it is sufficient to note that the Ti-rich regions predicted by the simulation are of a complex structure not resolved by the model, but expected to be essentially "intergranular" in nature.

By way of summarizing this section, we note that by incorporating the influence of grain boundaries, an unusual solute distribution can be thermodynamically rationalized by this model, and this aligns qualitatively with the experimental results presented earlier; we turn our attention to a quantitative comparison in the final section that follows. Before proceeding, we note that the total internal energy of the nanostructured W-20 at.% Ti alloy in Fig. 10 is calculated to be -440.76 kJ/mol, which is, in fact, lower than that of the bulk W-20 at.% Ti solid solution (Fig. 9) at -436.92 kJ/mol. The energy relief afforded by grain boundary-segregated states achieves a lower energy structure than any competing state on the bulk phase diagram.

7. Summary: Comparison of Experiments and Simulations

We have explored a W-20 at.% Ti alloy prepared by high-energy ball milling to achieve a nanostructured state, followed by annealing at 1100°C for one week to evolve an equilibrium structure. Unlike unalloyed W processed through a similar route, the W-Ti alloy is structurally stable over the course of the treatment at 1100°C, with grain size distributions before and after annealing that are quite similar and centered at about 20 nm. We attribute this to a nonuniform solute distribution that evolves upon annealing the alloy, which is summarized in Fig. 11 and 12 as a comparison among our experimental and simulation results. This comparison includes a STEM image with a Ti distribution overlay (Fig. 11(a)), chemical maps colored red for Ti and blue for W atoms (Fig. 11), and quantitative compositional line scans on easily comparable axes

(Fig. 12). The compilation of results in Fig. 11 and Fig. 12 underscores the major conclusions of this work:

- For the W-20 at.% Ti alloy equilibrated at 1100° C, the bulk phase diagram gives the expected stable state as a single-phase BCC solid solution. However, a nanoscale 20 nm grain structure with inhomogeneously-distributed Ti is observed by TEM, STEM (Fig. 11(a)), as well as APT (Fig. 11(b)).
- The heterogeneous distribution of Ti is consistent among both experimental methods shown in Fig. 11(a)-(b). Compositional line profiles in Fig. 12(a)-(b) show the maximum Ti content is well above the nominal concentration and as high as 50-60 at.%, and the minimum is around 0-5 at.%. The fluctuation in Ti concentration profiles shows an apparent periodicity similar to the tungsten grain size acquired by TEM measurement, which suggests that Ti atoms are depleted from W-rich grains and segregate to the intergranular regions; the characteristic length scale for W-rich grains is about ~20 nm.
- A kinetic analysis suggests that the diffusional distances accessible to this system are on the microscale and considerably larger than the nanoscale sizes of Ti depleted and enriched regions. The non-uniform solute distribution seen in Fig. 11(a)-(b) thus may not be simply a result of kinetic considerations.
- Our Monte Carlo simulations support a thermodynamic contribution to the stability of the nanostructure in this alloy. A simulated W-20 at.% Ti alloy equilibrated with grain boundary states at 1100°C evolves to a nanoscale structure that is remarkably consistent with the experimental observations. The conformity includes (a) the presence of W-rich BCC grains that are about 20-30 nm in characteristic size, and (b) a nonuniform solute distribution, shown visually in Fig. 11(c) and quantitatively in Fig. 12(c), that comprises peak Ti contents as high as 40-60 at.% and Ti-depleted regions of ~5 at.% Ti. We interpret the strong alignment of the simulations and experiments, summarized in Fig. 11-12, as evidence that grain boundary states and the tendency for Ti for intergranular segregation in W is at play in the thermal stability of this nanostructured alloy.

Acknowledgements

This work was primarily supported by the US Army Research Office, under grant No. W911NF-09-1-0422, with continuing support from the US Defense Threat Reduction Agency, under grant No. HDTRA1-11-1-0062.

References

[1] Detor AJ, Miller MK, Schuh CA. Philosophical Magazine 2006;86:4459.
[2] Dillon SJ, Tang M, Carter WC, Harmer MP. Acta Materialia 2007;55:6208.
[3] Liddicoat PV, Liao X-Z, Zhao Y, Zhu Y, Murashkin MY, Lavernia EJ, Valiev RZ, Ringer SP. Nature Communications 2010;1:63.
[4] Taheri ML, Sebastian JT, Reed BW, Seidman DN, Rollett AD. Ultramicroscopy 2010;110:278.
[5] Tang F, Gianola DS, Moody MP, Hemker KJ, Cairney JM. Acta Materialia 2012;60:1038.
[6] Cantwell PR, Tang M, Dillon SJ, Luo J, Rohrer GS, Harmer MP. Acta Materialia 2014;62:1.
[7] Weissmüller J. Nanostructured Materials 1993;3:261.
[8] Weissmüller J. Materials Science and Engineering: A 1994;179:102.
[9] Kirchheim R. Scripta Materialia 2006;55:963.
[10] Gottstein G, Shvindlerman L. Scripta Materialia 2006;55:965.
[11] Chookajorn T. Ph.D. Thesis, Department of Materials Science and Engineering: Massachusetts Institute of Technology, 2013.
[12] Chookajorn T, Schuh CA. Physical Review B 2014;89:064102.
[13] Chookajorn T, Murdoch HA, Schuh CA. Science 2012;337:951.
[14] Hayden HW, Brophy JH. Journal of The Electrochemical Society 1963;110:805.
[15] German RM, Munir ZA. Metallurgical and Materials Transactions A 1976;7:1873.
[16] Cliff G, Lorimer GW. Journal of Microscopy 1975;103:203.
[17] Jonsson S. Zeitschrift für Metallkunde 1996;87:784.
[18] Murray JL. Ti-W (Titanium-Tungsten). In: Massalski TB, editor. Binary Alloy Phase Diagrams, vol. 3. Materials Park, Ohio: ASM International, 1990. p.3494.
[19] Bellon P, Averback RS. Physical Review Letters 1995;74:1819.
[20] Jiang HG, Perez RJ, Lau ML, Lavernia EJ. Journal of Materials Research 1997;12:1429.
[21] Jiang HG, Hu HM, Lavernia EJ. Journal of Materials Research 1999;14:1760.
[22] Wu F, Bellon P, Melmed AJ, Lusby TA. Acta Materialia 2001;49:453.
[23] Lund AC, Schuh CA. Physical Review Letters 2003;91:235505.
[24] Odunuga S, Li Y, Krasnochtchekov P, Bellon P, Averback RS. Physical Review Letters 2005;95:045901.
[25] Wu F, Isheim D, Bellon P, Seidman DN. Acta Materialia 2006;54:2605.
[26] Delogu F. Journal of Applied Physics 2008;104:073533.
[27] Delogu F. Acta Materialia 2008;56:2344.
[28] Vo NQ, Odunuga S, Bellon P, Averback RS. Acta Materialia 2009;57:3012.
[29] Wang M, Vo NQ, Campion M, Nguyen TD, Setman D, Dillon S, Bellon P, Averback RS. Acta Materialia 2014;66:1.
[30] Atzmon M. Physical Review Letters 1990;64:487.
[31] Xu J, Collins GS, Peng LSJ, Atzmon M. Acta Materialia 1999;47:1241.
[32] Humphry-Baker SA, Schuh CA. Scripta Materialia 2011;65:516.
[33] Wang M, Averback RS, Bellon P, Dillon S. Acta Materialia 2014;62:276.
[34] Darken LS. Trans. Aime 1948;175:41.
[35] Rudd RE, Cabot WH, Caspersen KJ, Greenough JA, Richards DF, Streitz FH, Miller PL. Physical Review E 2012;85:031202.
[36] Chen Y, Schuh CA. Journal of Applied Physics 2007;101:063524.
[37] Lee JS, Minkwitz C, Herzig C. physica status solidi (b) 1997;202:931.

[38] Köhler U, Herzig C. physica status solidi (b) 1987;144:243.
[39] Murdoch HA, Schuh CA. Journal of Materials Research 2013;28:2154.
[40] Kwang Lee S, Nyung Lee D. Calphad 1986;10:61.
[41] de Boer FR. Cohesion in Metals: Transition Metal Alloys, 1988.
[42] Jones H. Metal Science 1971;5:15.
[43] Singman CN. Journal of Chemical Education 1984;61:137.
[44] Lassner E, Schubert W-D. Tungsten : properties, chemistry, technology of the element, alloys, and chemical compounds. New York: Kluwer Academic/Plenum Publishers, 1999.
[45] Senkov ON, Dubois M, Jonas JJ. Metall. Mater. Trans. A 1996;27:3963.
[46] Kaye GWC, Laby TH. Tables of physical and chemical constants and some mathematical functions: Longman, 1973.
[47] Luo Y-R. BDEs of Cr(Cr ±)-, Mo(Mo ±)-, and W(W ±)-X bonds. Comprehensive Handbook of Chemical Bond Energies CRC Press, 2007. p.713.
[48] Murdoch HA, Schuh CA. Acta Materialia 2013;61:2121.
[49] Luo J, Gupta VK, Yoon DH, Meyer HM. Applied Physics Letters 2005;87.
[50] Gupta VK, Yoon D-H, Meyer Iii HM, Luo J. Acta Materialia 2007;55:3131.

Figure Captions

Fig. 1. Characterization of pre-annealing structures. The bright-field TEM images with a dark-field TEM inset of (a) unalloyed W and (b) W-20 at.% Ti confirm a nanoscale grain size distribution in the as-milled state. The electron diffraction patterns of the as-milled structures from both (c) unalloyed W and (d) W-20 at.% Ti show fairly complete rings of diffraction spots, indexed by the Miller indices of BCC W, as expected from fine-grained polycrystalline materials.

Fig. 2. Characterization of post-annealing structures. (a) After a one-week anneal at 1100°C, the FIB image of unalloyed W shows a coarsened grain structure with grain sizes reaching the microscale. (b) The bright-field TEM image (with a dark-field TEM inset) of W-20 at.% Ti after the same annealing condition shows a nanoscale grain structure with grain sizes similar to the as-milled structure. The electron diffraction data obtained from unalloyed W after annealing (c) become more sparse and spot-like, whereas those obtained from W-20 at.% Ti (d) show complete rings of diffracted signal.

Fig. 3. Grain size distribution histograms of unalloyed W and W-20 at.% Ti before and after a one-week anneal at 1100°C. The average initial grain sizes in the as-milled state are around 20 nm and remain smaller than 100 nm in the annealed W-20 at.% Ti. On the other hand, the grain sizes of the unalloyed W after annealing become larger than 100 nm, with the upper limit extending into the micrometer range.

Fig. 4. (a) A STEM image and the associated STEM-EDS mixed, W, and Ti elemental maps of the as-milled W-20 at.% Ti alloy. (b) EDS compositional line scans show a distribution of titanium with some fluctuation around 20 at.% that does not correlate well with changes in the STEM contrast above it.

Fig. 5. (a) A STEM image and the associated STEM-EDS mixed, W, and Ti elemental maps of the W-20 at.% Ti alloy after a one-week anneal at 1100°C. (b) EDS compositional line scans confirm chemical segregation and illustrate depletion of titanium from regions of darker STEM contrast.

Fig. 6. Through-thickness representation of (a) mixed W and Ti elemental map and separated (b) W and (c) Ti distributions from atom probe tomography analysis of W-20 at.% Ti alloy after a one-week anneal at 1100°C. Titanium atoms display a spatial nonuniformity with a depletion-zone size comparable to the tungsten grain size.

Fig. 7. Quantitative volume distribution of Ti in the annealed W-20 at.% Ti alloy APT specimen. (a) Composition isosurfaces of W and Ti show depletion of Ti below the nominal concentration of 20 at.% in blue and enrichment of Ti above 20 at.% in red. (b) The three-dimensional view of the isosurfaces is presented for the whole specimen volume. The volume distribution of Ti is represented by the isovolume with the highest local Ti content in red and the lowest local Ti content in blue in equivalent planar (c) and three-dimensional (d) views. Compositional line profiles across the horizontal (e) and vertical (f) axes of the annealed W-20 at.% Ti atom probe specimen are also provided.

Fig. 8. Diffusivity and one-week diffusion distance at 1100°C of polycrystalline W self-diffusion and W-Ti interdiffusion as a function of average grain size. For W diffusion, the effective diffusivity is shown with isolated constituent diffusion paths.

Fig. 9. Equilibrium bulk W-20 at.% Ti structure at 1100°C calculated using the Monte Carlo alloy simulation. The structure is a single-phase solid solution since grain boundaries are not allowed in the present case. (a) The solute distribution map shows regions with all W atoms in black, those with all Ti atoms in white, and those with both of W-Ti in a composition-dependent shade of gray (b) The Ti composition profile shows minor fluctuations around the 20 at.% nominal concentration. Simulations are performed on a 400 x 400 x 6 BCC lattice with ΔH^{mix} = 20 kJ/mol.

Fig. 10. Equilibrium nanostructure of W-20 at.% Ti at 1100°C calculated using the Monte Carlo alloy simulation. With grain boundaries permitted to appear as potential equilibrium features, the alloy displays a complex segregation structure of Ti atoms around W-rich crystalline regions. (a) The solute distribution map illustrates an inhomogeneous distribution of Ti atoms. (b) The grain structure shows several nanoscale crystallites being dispersed in a matrix of intergranular matter. (c) The through-thickness compositional profile across the horizontal line shows peaks in local Ti content up to 60 at.% and valleys near zero. (d) The combined grain-atomic structure shows evident segregation of Ti atoms in black away from W-rich crystallites into the intergranular region. Detailed view along a horizontal line of the grain structure (e) and the chemical map (f) showing Ti-rich regions in bright contrast. Simulations are performed on a 400 x 400 x 6 BCC lattice with ΔH^{mix} = 20 kJ/mol and ΔH^{seg} = 50 kJ/mol.

Fig. 11. Comparison of the W-20 at.% Ti alloy structures after an equilibration at 1100°C from STEM-EDS analysis, atom probe tomography, and Monte Carlo alloy simulation. (a) An EDS elemental map with W atoms in blue and Ti atoms in red is shown on the left, and a grayscale STEM image with an overlaying EDS map of Ti in red is shown on the right. (b) The through-thickness chemical distribution from atom probe tomography displays W atoms in blue and Ti atoms in red. (c) A chemical map obtained from Monte Carlo simulation showing Ti atoms in red and W atoms in blue is presented as a comparison to the W-Ti EDS map and the APT chemical distribution.

Fig. 12. A heterogeneous distribution of Ti is confirmed by all three independent methods. The Ti composition line scans from (a) STEM-EDS, (b) atom probe tomography, and (c) Monte Carlo alloy simulation all reveal a similar Ti segregation profile, with the fluctuation up to about 60 at.% and a periodicity comparable to the average tungsten grain size of around 20 nm. Ti is presented in red.

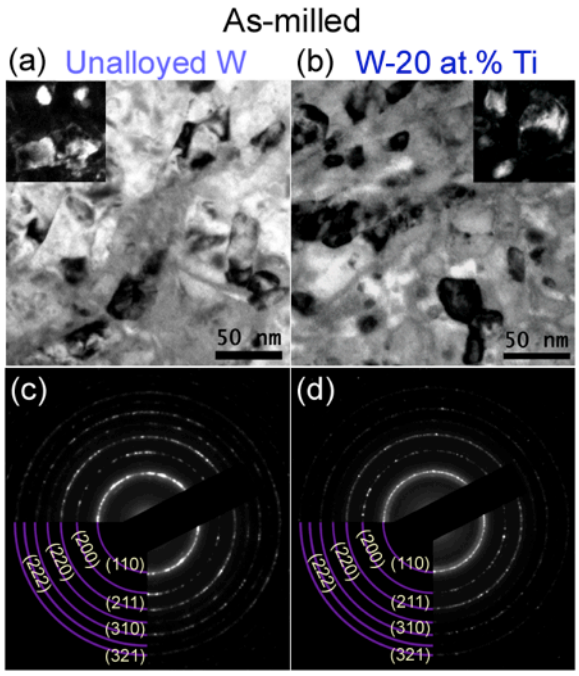
As-milled
(a) Unalloyed W
(b) W-20 at.% Ti
50 nm
50 nm
(c)
(d)
(200)
(110)
(220)
(211)
(222)
(310)
(321)
(200)
(110)
(220)
(211)
(222)
(310)
(321)

Fig. 1

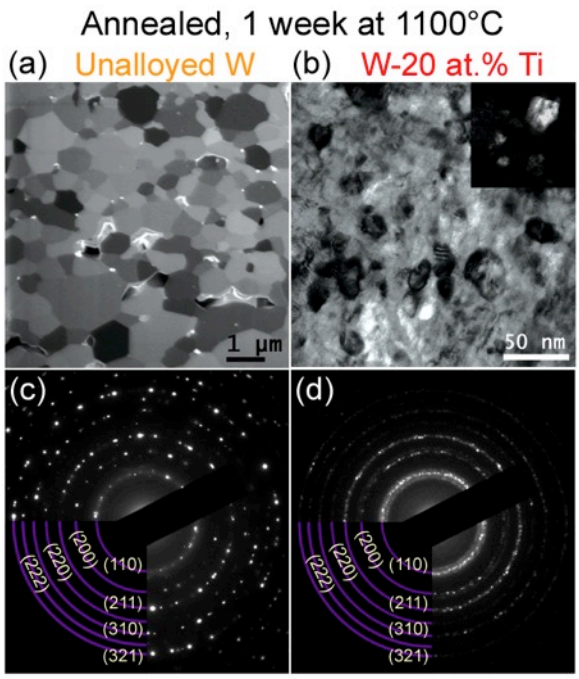
Annealed, 1 week at 1100°C
(a) Unalloyed W
(b) W-20 at.% Ti
1 μm
50 nm
(c)
(d)
(222)
(220)
(200)
(110)
(211)
(310)
(321)

Fig. 2

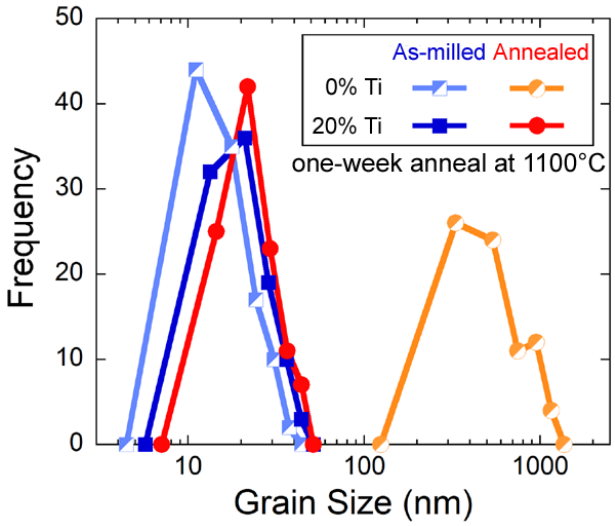
As-milled Annealed
0% Ti
20% Ti
one-week anneal at 1100°C
Frequency
Grain Size (nm)
0
10
20
30
40
50
10
100
1000

Fig. 3

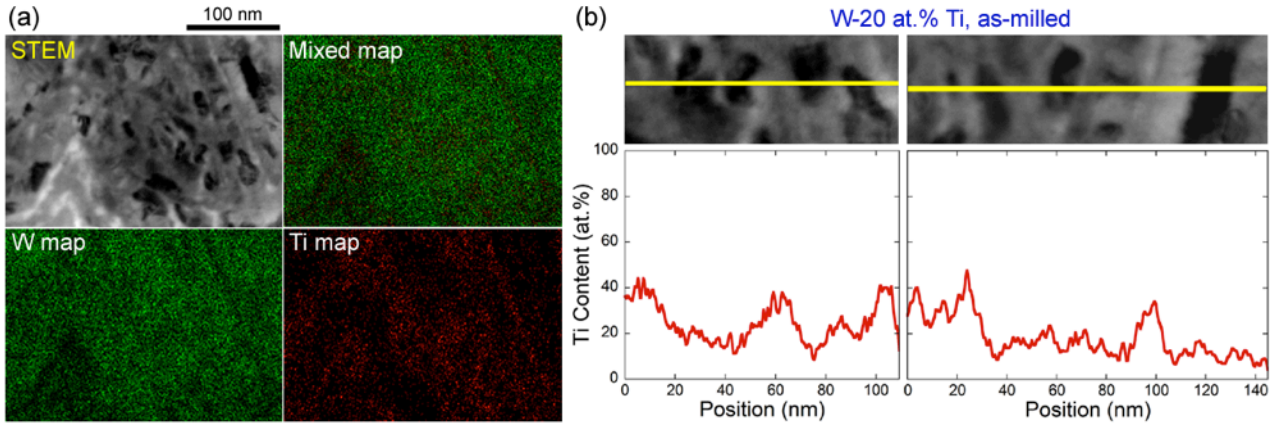
(a)
100 nm
STEM
Mixed map
W map
Ti map
(b)
W-20 at.% Ti, as-milled
Ti Content (at.%)
Position (nm)
Position (nm)

Fig. 4

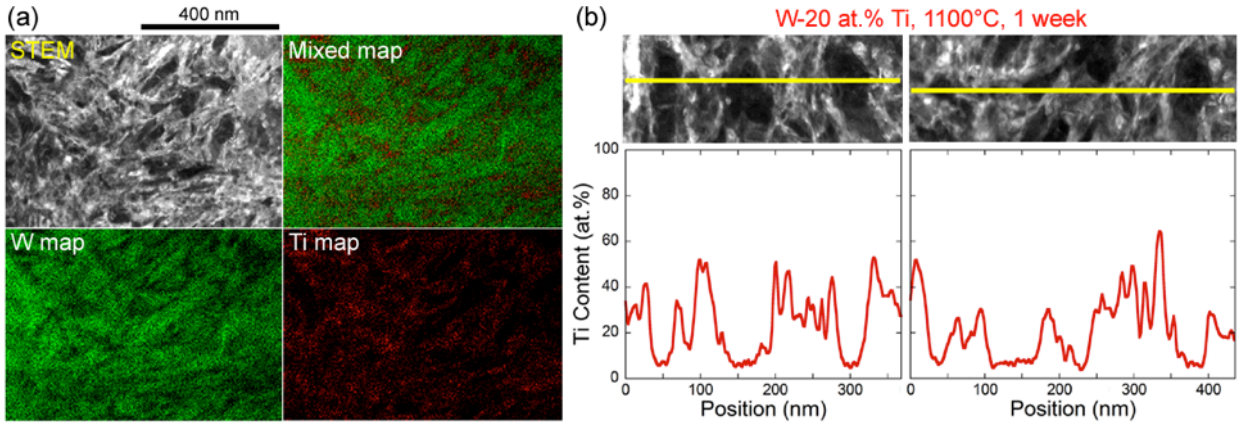
(a)
400 nm
STEM
Mixed map
W map
Ti map
(b)
W-20 at.% Ti, 1100°C, 1 week
Ti Content (at.%)
Position (nm)
Position (nm)

Fig. 5

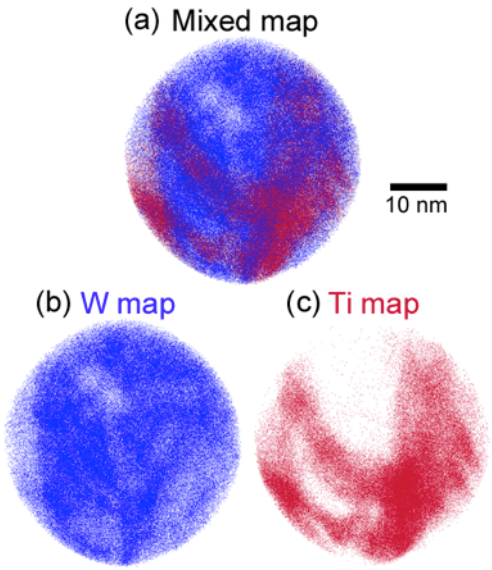

Fig. 6

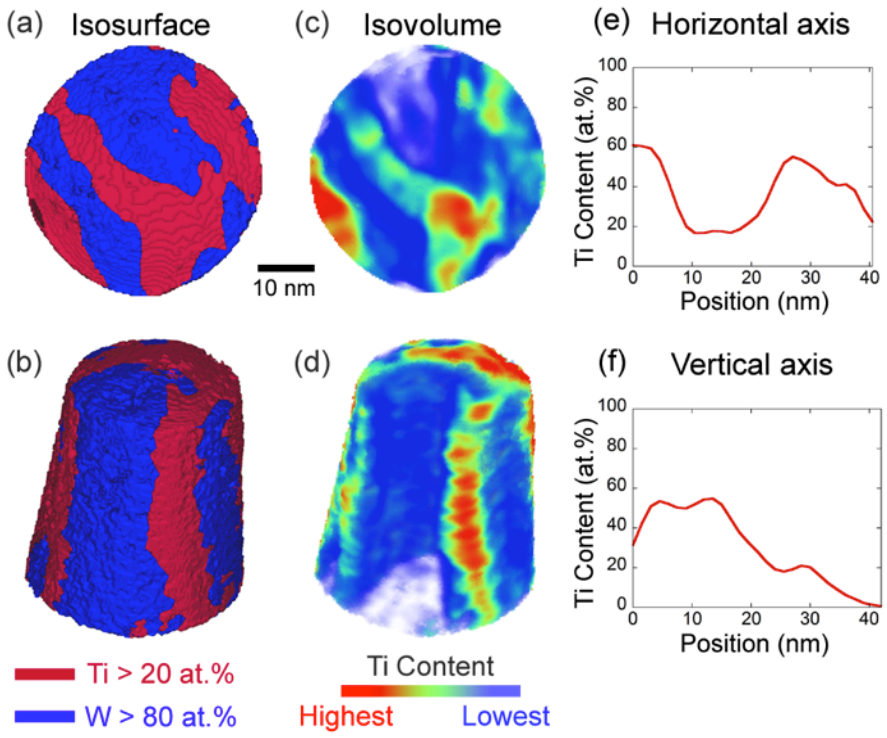
(a) Isosurface
(c) Isovolume
(e) Horizontal axis
10 nm
Ti Content (at.%)
Position (nm)
(b)
(d)
(f) Vertical axis
Ti > 20 at.%
W > 80 at.%
Ti Content
Highest
Lowest

Fig. 7

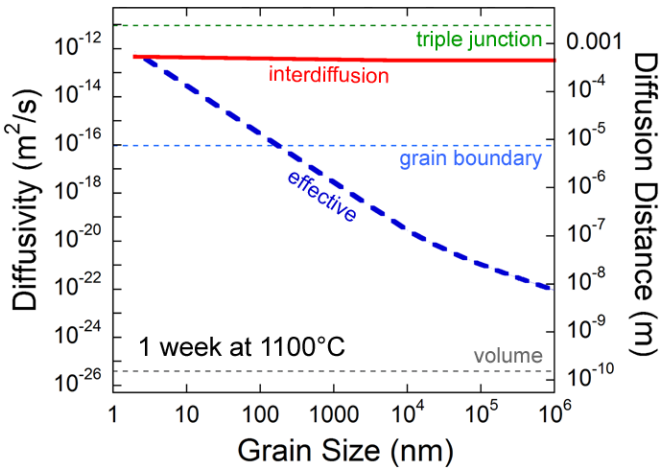
triple junction
interdiffusion
grain boundary
effective
volume
1 week at 1100°C
Diffusivity (m²/s)
Diffusion Distance (m)
Grain Size (nm)
10⁻¹²
10⁻¹⁴
10⁻¹⁶
10⁻¹⁸
10⁻²⁰
10⁻²²
10⁻²⁴
10⁻²⁶
0.001
10⁻⁴
10⁻⁵
10⁻⁶
10⁻⁷
10⁻⁸
10⁻⁹
10⁻¹⁰
1
10
100
1000
10⁴
10⁵
10⁶

Fig. 8

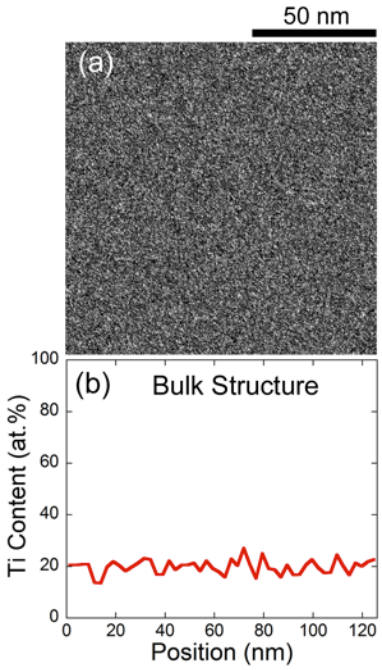
50 nm
(a)
100
(b)
Bulk Structure
Ti Content (at.%)
80
60
40
20
0
0
20
40
60
80
100
120
Position (nm)

Fig. 9

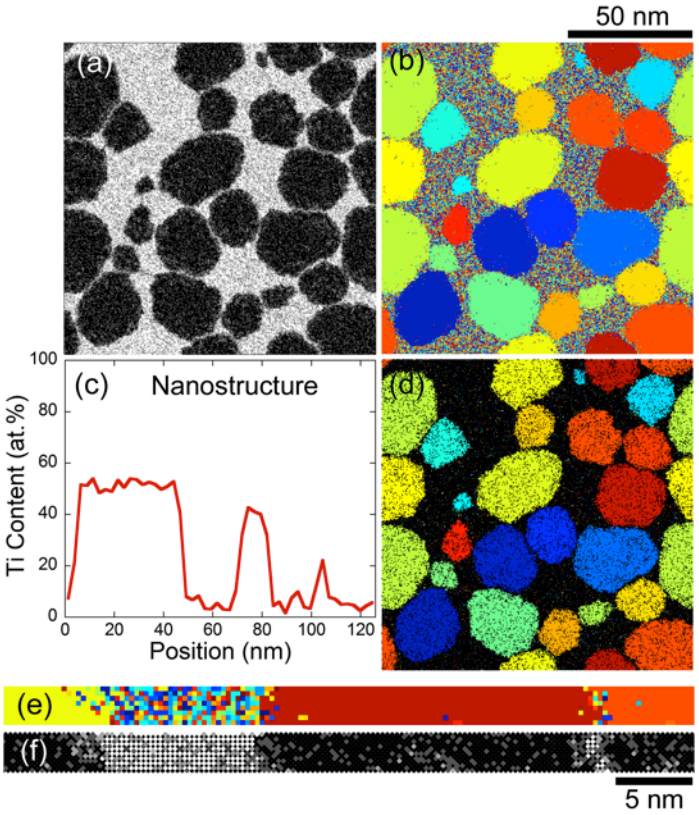

Fig. 10

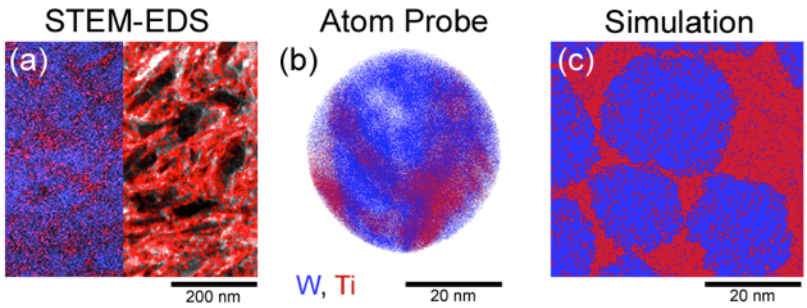

Fig. 11

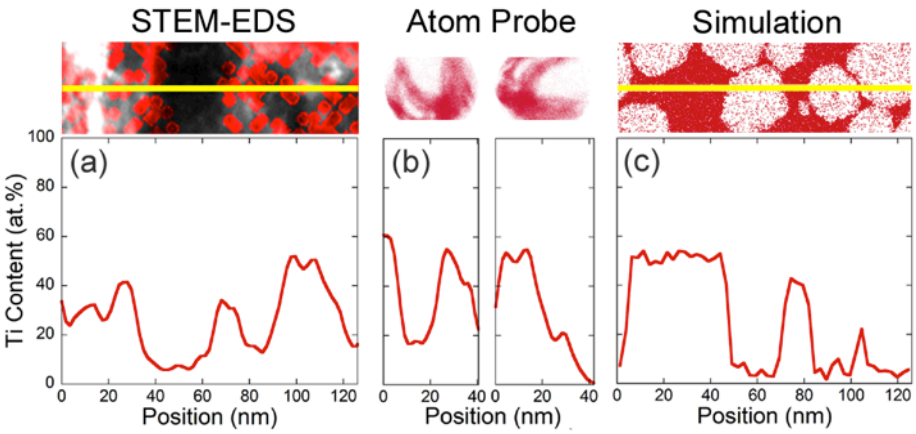
STEM-EDS
Atom Probe
Simulation
(a)
(b)
(c)
Ti Content (at.%)
Position (nm)
Position (nm)
Position (nm)

Fig. 12